

Article

Predicting the Temperature-Dependent Long-Term Creep Mechanical Response of Silica Sand-Textured Geomembrane Interfaces Based on Physical Tests and Machine Learning Techniques

Zhiming Chao ^{1,2,3,†}, Haoyu Wang ³, Hanwen Hu ^{4,†}, Tianchen Ding ⁴ and Ye Zhang ^{4,*}¹ Shanghai Estuarine and Coastal Science Research Center, Shanghai 201201, China² Institute of Water Sciences and Technology, Hohai University, Nanjing 211106, China³ College of Ocean Science and Engineering, Shanghai Maritime University, Shanghai 200135, China⁴ Mentverse Ltd., 25 Cabot Square, Canary Wharf, London E14 4QZ, UK

* Correspondence: ye.zhang@mentverse.co.uk; Tel.: +44-7557782175

† These authors contributed equally to this work.

Abstract: Precisely assessing the creep mechanical response of sand–geomembrane interfaces is vital for the design of relevant engineering applications, which is inevitable to be influenced by temperature and stress statuses. In this paper, based on the self-developed temperature-controlled large interface shear apparatus, a series of long-term creep shear tests on textured geomembrane–silica sand interfaces in different temperatures, normal pressure, and creep shear pressure were conducted, and a database compiled from the physical creep shear test results is constructed. By adopting the database, three disparate machine learning algorithms of the Back Propagation Artificial Neural Network (BPANN), the Support Vector Machine (SVM) and the Extreme Learning Machine (ELM) were adopted to assess the long-term creep mechanical properties of sand–geomembrane interfaces while also considering the influence of temperature. Then, the forecasting results of the different algorithms was compared and analyzed. Furthermore, by using the optimal machine learning model, sensitivity analysis was carried out. The research indicated that the BPANN model has the best forecasting performance according to the statistics criteria of the Root-Mean-Square Error, the Correlation Coefficient, Wilmot’s Index of Agreement, and the Mean Absolute Percentage Error among the developed models. Temperature is the most important influence factor on the creep interface mechanical properties, followed with time. The research findings can support the operating safety of the related engineering facilities installed with the geomembrane.

Keywords: sand; creep shear mechanical response; SVM; BPANN

Citation: Chao, Z.; Wang, H.; Hu, H.; Ding, T.; Zhang, Y. Predicting the Temperature-Dependent Long-Term Creep Mechanical Response of Silica Sand-Textured Geomembrane Interfaces Based on Physical Tests and Machine Learning Techniques. *Materials* **2023**, *16*, 6144. <https://doi.org/10.3390/ma16186144>

Academic Editor: Krzysztof Schabowicz

Received: 14 August 2023

Revised: 5 September 2023

Accepted: 7 September 2023

Published: 10 September 2023



Copyright: © 2023 by the authors. Licensee MDPI, Basel, Switzerland. This article is an open access article distributed under the terms and conditions of the Creative Commons Attribution (CC BY) license (<https://creativecommons.org/licenses/by/4.0/>).

1. Introduction

As an excellent water-proofing material, geomembrane is extensively used as construction material in various engineering applications [1–5]. With the development of a geomembrane manufacturing technology, different types of this material are available. Among them, textured geomembrane is the most popular in practical engineering applications because textured geomembrane can form a strong interface mechanical performance when in contact with other construction material, such as soil, due to the existence of texture on the geomembrane surfaces [6,7]. Although compared to other types of geomembrane, the interfaces between textured geomembrane and soil have better stability, but the textured geomembrane–soil interface is still the weakest component in engineering facilities [8–13]. Thus, the correct estimation of the interface mechanical properties between textured geomembrane and soil is critical for the operating safety of relative engineering facilities.

In general, the service life of geomembrane in engineering infrastructure is over decades [14,15]. During the operation of engineering applications, the textured geomembrane–soil interface is often subjected to constant creep shear stress resulting from the overlaying construction material [16,17]. The long-term creep interface deformation has an obvious difference with the short-term deformation caused by the rapid loading of shear stress. The occurrence of creep shear deformation is more hidden and the deformation can rise rapidly in a short period, which has a more significant hazard on the safety of engineering facilities [18,19]. It highlights the necessity of precisely predicting the long-term creep mechanical response of textured geomembrane–soil interfaces.

In reality, the engineering environment is complex, and the buildings installed with geomembrane are often subjected to temperature loadings [20–25]. For example, due to the exothermal reaction of buried waste biodegradation, the inside temperature of landfills can reach 60–80 °C [26,27]. As a common water-proofing material, it is inevitable that geomembrane installed in landfills will experience a high temperature environment. Since the main raw material of producing geomembrane is thermal-softening plastic materials such as nylon, polyethylene, etc., in elevated temperatures, the softening of geomembrane may occur [28]. This has an obvious influence on the interface mechanical properties between geomembrane and soil [16]. Especially for textured geomembrane, the softening of texture can remarkably change the interaction between geomembrane and soil to result in a considerable impact on the interface's mechanical response [29,30]. However, due to the limitation of the temperature-controlled interface shear apparatus, at present, the research involving the assessment of the temperature-dependent mechanical properties for geomembrane–soil interfaces is rare, let alone the investigation about the long-term creep mechanical behavior of textured temperature–soil interfaces by considering the temperature effects.

The interaction between textured geomembrane and soil is complicated, which leads to the multiple influence factors on the mechanical performance of textured geomembrane–soil interfaces [31–33]. Especially for the temperature-dependent creep shear mechanical response, it requires to consider the factors of time and temperature, which further increases the complexity of the interface action mechanism. The complex interaction and multiple impact factors cause the difficulty of predictive modelling for the long-term creep mechanical behavior of textured geomembrane–soil interfaces by considering the temperature effects and adopting the traditional estimation methods, such as the mathematical statistical approach, etc. [15,34]. Due to the development in computer technology, in recent years, the machine learning techniques are extensively adopted to replicate the complex action mechanism by considering multiple influence factors [30,35–41]. In the field of civil engineering, machine learning modeling techniques have found widespread use, including but not limited to the following:

- (1) estimating rock permeability [42,43];
- (2) predicting interface shear strength [44–46];
- (3) assessing cement mortar permeability [47,48].

The existing research manifesting the machine learning methods can describe the complex relationships between plentiful factors with high precision and efficiency. However, in the published research, the investigation involving the modelling of the temperature-dependent long-term creep mechanical response of the textured geomembrane–soil interface by adopting machine learning techniques is not reported.

In this paper, the effectiveness of the three disparate machine learning algorithms in assessing the temperature–dependent long-term creep interface mechanical response between textured geomembrane and silica sand are compared and analyzed, including the Backpropagation Artificial Neural Network (BPANN), the Support Vector Machine (SVM), and the Extreme Learning Machine (ELM). Moreover, by using the optimal machine learning predictive model, the sensitivity analysis of different influence factors on the creep shear mechanical response of textured geomembrane–silica sand interfaces is conducted to determine the relative importance. The research outcomes can provide an effective tool for

estimating the temperature-dependent long-term creep mechanical properties of textured geomembrane–sand interfaces, which can provide a reference for the construction of related engineering services.

2. Physical Experiment

To obtain the data for machine learning modeling, a self-developed large interface direct shear apparatus was utilized, and the tested geomembrane is shown in Figure 1. The temperature-controlled creep shear tests on silica sand–textured geomembrane interfaces were conducted at 25 kPa, 50 kPa, and 100 kPa under normal stress, and the creep shear stress level was 50%, 70%, and 90% of the monotonic peak shear strength for the interface under the corresponding normal stress. For each test condition, three different temperatures of 30 °C, 60 °C, and 200 °C were adopted. The specific test procedure is as follows:

- (1) Textured geomembrane and silica sand sample was installed;
- (2) The interface temperature was adjusted to the predetermined value and kept stable during the whole test;
- (3) The interface was consolidated under the corresponding normal stress for 12 h;
- (4) A certain shear stress was imposed on the interfaces and kept stable during the whole test;
- (5) The test was terminated until the interface failed or the test duration (6 days) ran out.

The properties of the test material are listed in Table 1, and the test scheme is shown in Table 2.

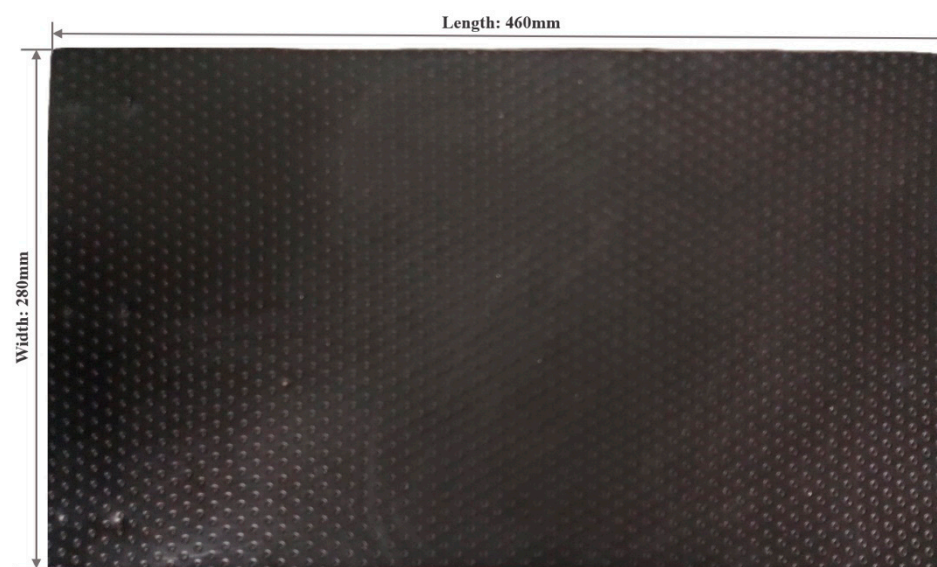


Figure 1. The tested textured geomembrane.

Table 1. The properties of the test sample.

Textured geomembrane (Flat die extruded)	Thickness (mm)	2.0
	Textured height (mm)	0.26
	Fracturing strength (N/mm)	16.2
	Yield strength (N/mm)	22.3
	Yield elongation rate (%)	12.2
	Fracturing elongation rate (%)	120
	Puncture strength (N)	195
Silica sand	Particle size range (mm)	0.075~2
	Density (g/cm ³)	1.50
	Optimum water content (%)	10
	Uniformity coefficient	3.327
	Curvature coefficient	0.3
	Median particle size (mm)	0.785

Table 2. Test scheme.

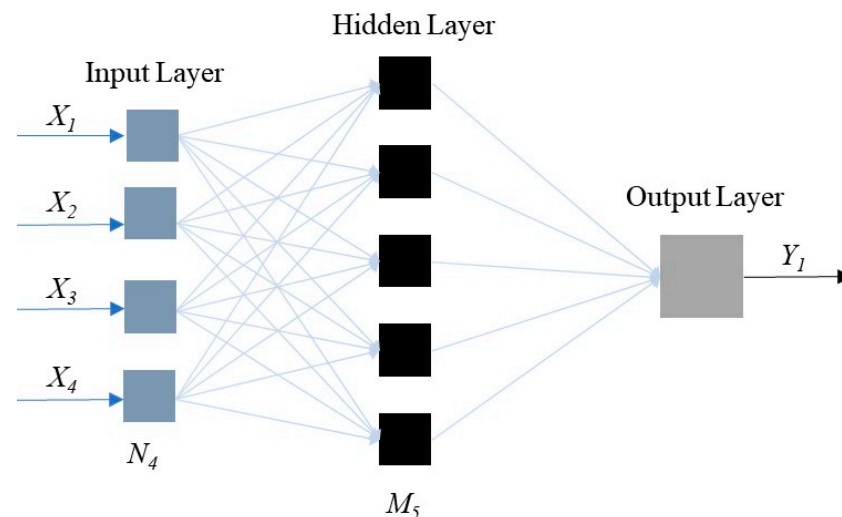
Test Sample	Normal Pressure (kPa)	Temperature (°C)	Creep Shear Stress
Silica sand–textured geomembrane interface	25, 50, 100	30, 60, 200	50%, 70%, and 90% of the monotonic interface peak shear strength

3. Machine Learning Algorithm

By adopting the afore physical test results, three different kinds of machine learning algorithms, BPANN, SVM and ELM, were selected to establish the predictive models on the temperature-dependent creep shear mechanical response of textured geomembrane–sand interfaces by adopting the program software Matlab_R2022b_Windows. The introduction of the adopted machine learning algorithms is presented below.

3.1. BPANN

Artificial Neural Network is the most prevalent machine learning algorithm, which can be divided as different kinds [49–51]. Among them, the BPANN is the most extensively adopted in civil engineering areas [10,52]. The BPANN model is composed of the input, hidden, and output layers. In this research, the input parameters are normal pressure, creep shear stress, temperature, and time, which corresponds to four joints in the input layer. The output parameter is the creep shear displacement, which corresponds to one joint in the output layer. The joint number of the hidden layer is ascertained by adopting the exhaustive approach, which is 5 in this research. The schematic diagram of the adopted BPANN model structure is shown in Figure 2. The activation function and network training algorithm in the BPANN model adopts the Hyperbolic Tangent Sigmoid Transfer Function and the Levenberg-Marquardt Backpropagation Algorithm, respectively.

**Figure 2.** The schematic diagram of BPANN model.

3.2. SVM

SVM is another widely adopted machine learning algorithm, which can describe the complex relationship between multiple variables based on the limited number of sample data [53,54]. Also, SVM can project low-dimensional data to high-dimensional data by adopting the kernel function so that the non-linear modelling can be transformed into linear modelling [55,56]. Additionally, SVM can adopt the k-fold cross-validation method (k-CV) in conducting modelling. The theory of k-CV is to divide the original data as equal groups. Among the groups, k-1 groups are adopted as the training data, and the left group

is adopted for validation. By selecting different data groups as the testing dataset, the train and validation procedure is repetitive with k times, and the average predictive outcomes of the k times are used as the final value. In this research, the value of k is taken as 10.

3.3. ELM

ELM originates from the ANN model, with the structure being similar with the feedforward ANN [57]. However, in some cases, compared to the ANN model, ELM can achieve complex modelling in a short period, with low computation cost. Like ANN, the joint number of the ELM hidden layer also impacts the forecasting behavior significantly. Therefore, the same exhaustive method is adopted to determine the hidden layer joint number in ELM as 5. For the input and output layer joint number, they are 4 and 1, corresponding to the four input parameters and one output parameter, respectively. The activation function adopts the Logarithmic Sigmoid Function.

4. Machine Learning Modelling

4.1. Establishment of the Database

Based on the aforementioned test results, the database was established. The database includes 27,000 datasets. Each dataset consists of four input parameters of normal pressure, creep shear pressure, time, and temperature, and one output parameter of creep shear displacement. The range of normal pressure is from 25 kPa to 100 kPa, and the time is from 0 min to 8640 min, with the temperature ranging from 30 °C to 200 °C. The parameters were chosen because they have large influence on the creep mechanical response of textured geomembrane–soil interfaces, as indicated by the existing research [1,58]. The statistics for the input and output parameters is listed in Table 3. The data distribution for the database is shown in Figure 3, with the x -axis and the y -axis representing the value of the input parameters and the corresponding data group number, respectively.

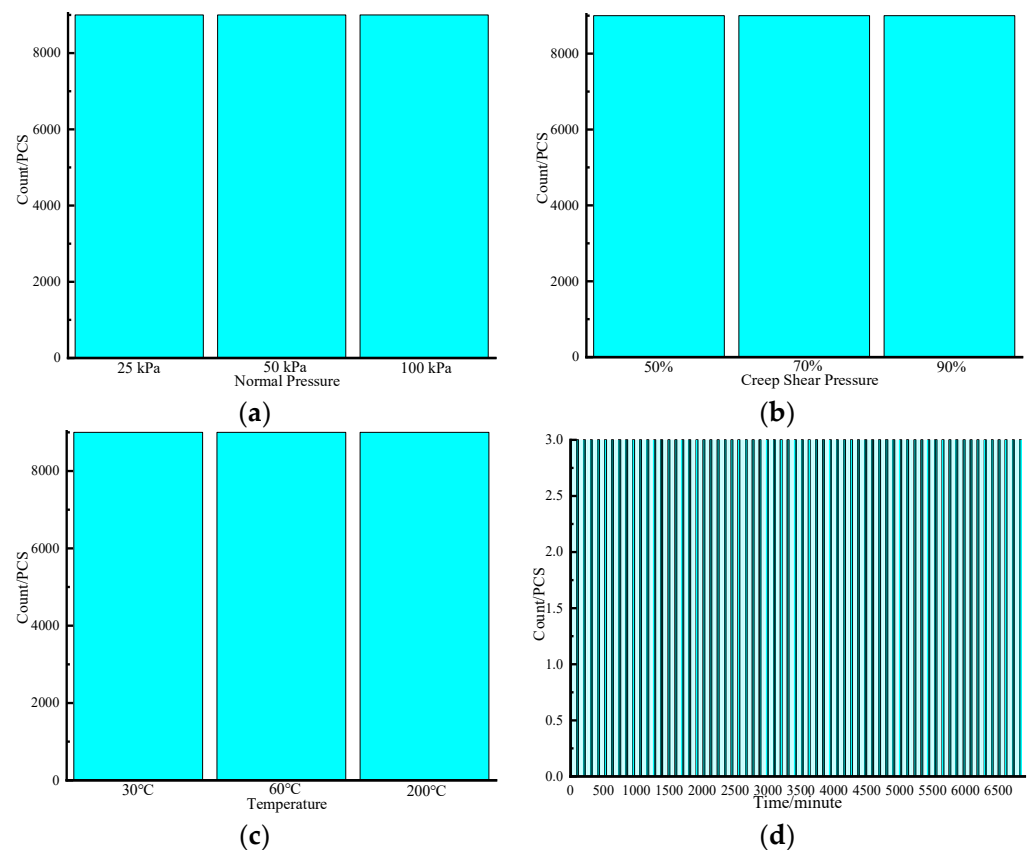


Figure 3. Data distribution of the complied database. (a) Normal pressure; (b) creep shear pressure; (c) temperature; and (d) time.

Table 3. The statistics.

	Parameters	Minimum Value	Maximum Value	Mean Value	Standard Deviation
Input	Normal pressure (kPa)	25	100	59	30.6
	Creep shear pressure	50% of the peak shear strength	90% of the peak shear strength	70% of the peak shear strength	20.39
	Time (minute)	0	8640	4320	650
	Temperature (°C)	30	200	95	20.72
Output	Creep shear displacement (mm)	0	47.20	24.50	6.40

4.2. Data Processing

Before machine learning modelling, it was required to divide the database into the training data, to train the models, and the testing data, to validate the predictive performance of the models. In this paper, the division ratio is set as 80% (21,600 groups) for the training data and 20% (5400 groups) for the testing data. Also, to improve the predictive precision and efficiency, the input data were normalized by adopting Equation (1).

$$x_{Normalised} = \frac{2(x - x_{min})}{x_{max} - x_{min}} - 1 \quad (1)$$

where $x_{Normalised}$ and x indicates the normalized and original values, respectively, and x_{min} and x_{max} indicates the minimum and maximum values, respectively.

4.3. Precision Assessment Indexes

To quantitatively analyze the forecasting accuracy of the constructed machine learning models, the following four assessment indexes were adopted: Root-Mean-Square Error (RMSE), Coefficient of Determination (R^2), Mean Absolute Percentage Error (MAPE), and Wilmot's Index of Agreement (WI), as presented in Equations (2)–(5).

$$RMSE = \sqrt{\frac{\sum_{i=1}^n (y_i - f_i)^2}{n}} \quad (2)$$

where n indicates the data number, y_i indicates the measured data, and f_i indicates the assessing value. The less the RMSE value is, the more precise the model.

$$R^2 = 1 - \frac{\sum_{i=1}^n (y_i - f_i)^2}{\sum_{i=1}^n (y_i - \bar{y})^2} \quad (3)$$

where \bar{y} indicates the average measured value.

$$MAPE = \frac{100\%}{n} \sum_{i=1}^n \frac{|y_i - f_i|}{y_i} \quad (4)$$

$$WI = 1 - \frac{\sum_{i=1}^n (y_i - f_i)^2}{\sum_{i=1}^n (|f_i - \bar{y}| + |y_i - \bar{y}|)^2} \quad (5)$$

5. Result and Analysis

5.1. Determining the Optimal Hidden Layer Joint Number

As aforementioned, the hidden layer joint number has a significant influence on the assessing results of the BPANN and ELM models. To determine the optimum number of hidden layer joints, the exhaustive approach was adopted with RMSE as the assessment index. The results are shown in Figure 4.

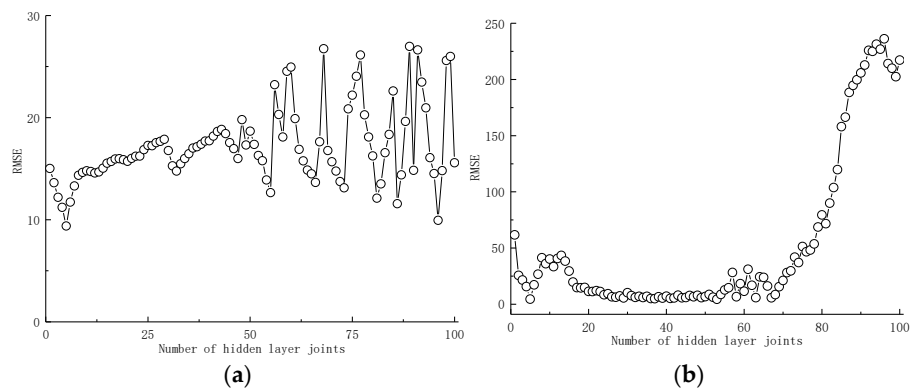


Figure 4. The optimization process. (a) BPANN; and (b) ELM.

Based on Figure 4, the hidden layer joint number has a considerable impact on the RMSE value of the BPANN and ELM models, ranging from 4.23 to 26.97 and from 236.24 to 4.51, respectively. By comparing the assessing results of the BPANN and ELM models containing various hidden layer joint numbers, it is found that when the hidden layer joint number is 5, both the BPANN and ELM models reach the high estimation precision of 4.23 and 4.51, respectively. Thus, in this research, both the BPANN and ELM models adopt five hidden layer joints.

5.2. Assessment Results of Various Machine Learning Models

The forecasting precision of different machine learning models on the train and test datasets, based on the indexes of RMSE, MAPE, WI, and R^2 , is shown in Figures 5–8.

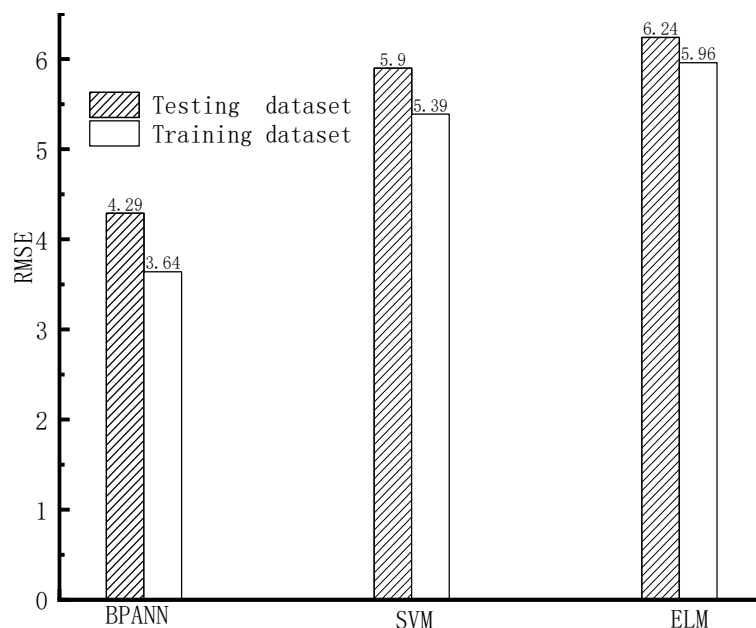


Figure 5. RMSE value.

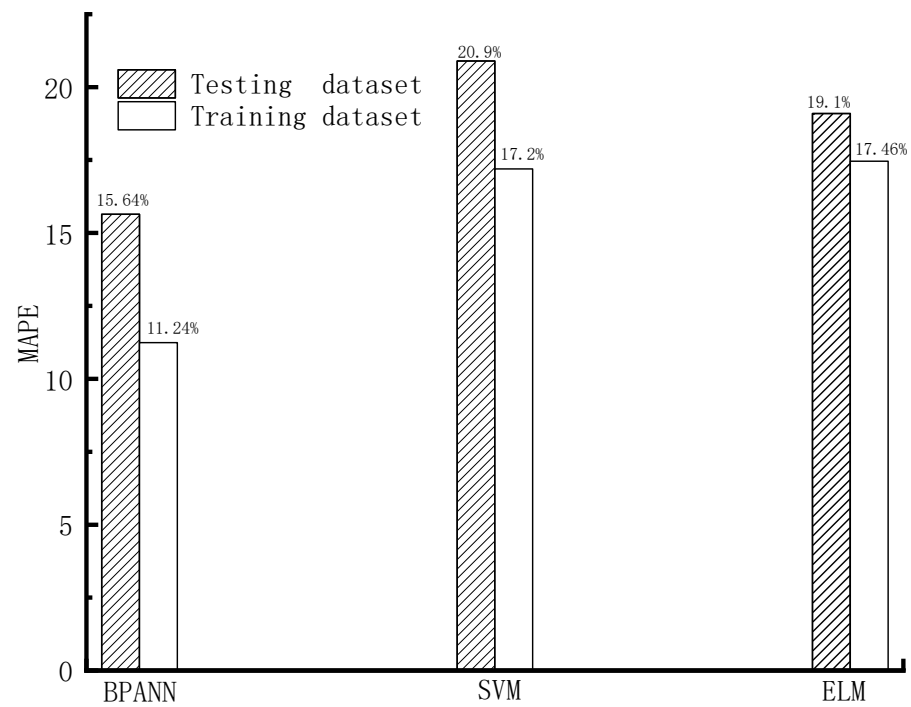


Figure 6. MAPE value.

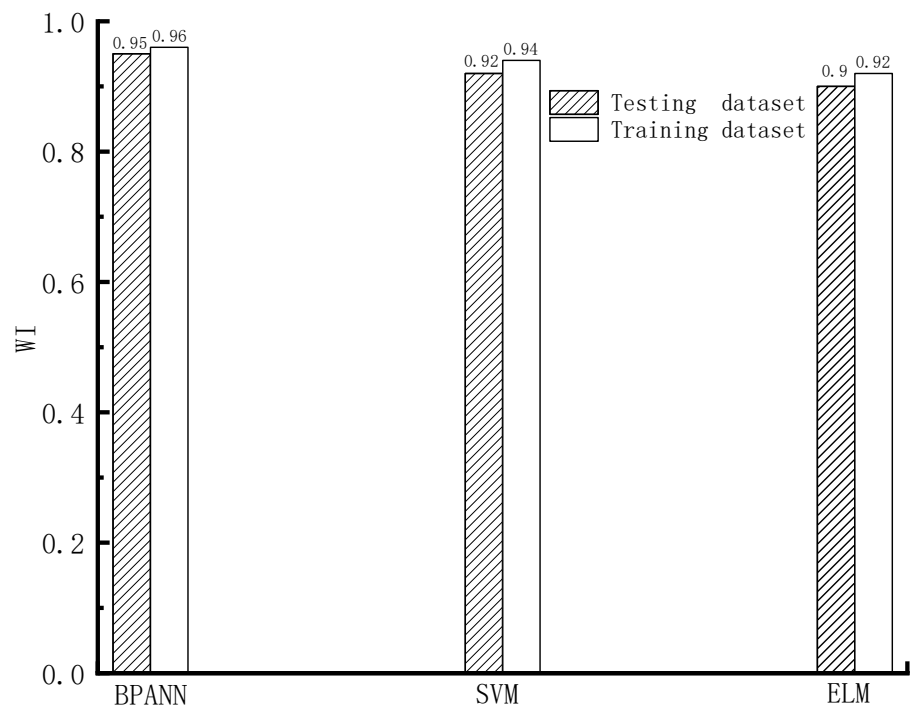


Figure 7. WI value.

As shown in Figures 5–8, based on the assessment indexes of RMSE, MAPE, WI, and R^2 , the assessing precision of the BPANN model is the highest among the models in the aspect of assessing the training dataset. In the quantitative analysis, the BPANN model achieved the lowest RMSE (3.64) and MAPE (11.24%) and the largest R^2 (0.99) and WI (0.96). It is followed by the SVM model, and its forecasting performance is better than the ELM model. For example, the RMSE value and the MAPE value of the ELM model (5.96 and 17.46%, respectively) is higher than that of the SVM model (5.39 and 17.2%, respectively).

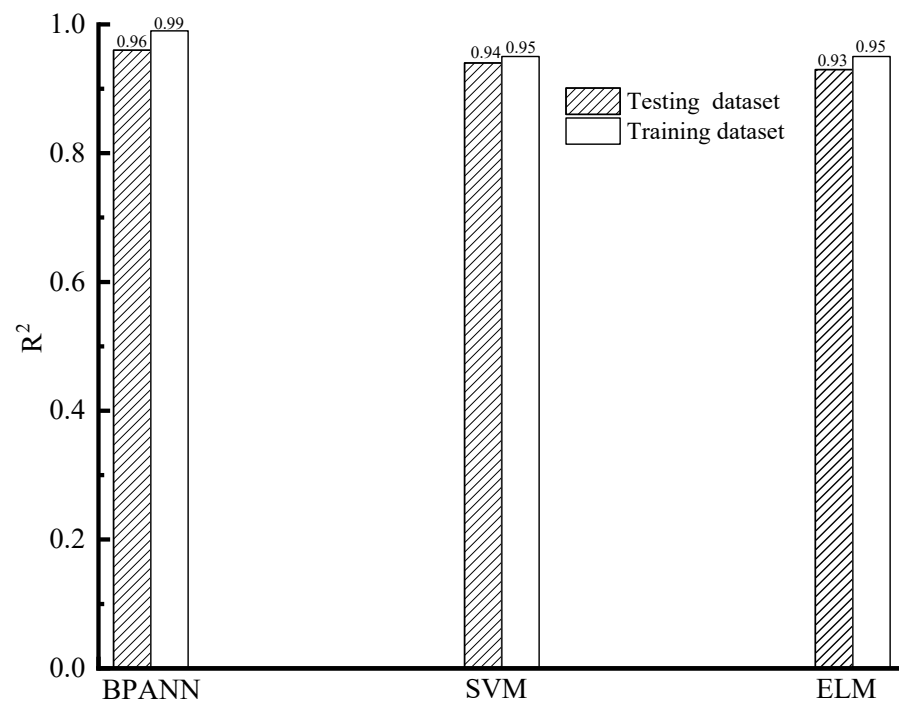


Figure 8. R² value.

In the aspect of the forecasting behavior on the testing datasets, as presented in Figures 5–8, like the outcomes on the training datasets, the assessing precision of the BPANN model is the best among the different algorithms. More specifically, among the models, the RMSE and MAPE values of the BPANN model is the most low, with 4.29 and 15.64%, respectively, and the R² and WI values of the BPANN model is the largest, with 0.96 and 0.95, respectively. For the SVM and ELM models, their forecasting performance is different based on the different assessment indexes. For example, the RMSE value of the ELM model (6.24) is higher than that of the SVM model (5.9), which indicates the superior performance of the SVM model than the ELM model. In comparison, the MAPE value of the ELM model (19.1%) is less than that of the SVM model (20.9%), which indicates the better precision of the ELM model than that of the SVM model.

5.3. Sensitivity Analysis

To investigate the relative significance of different factors on influencing the creep shear mechanical response of textured geomembrane–silica sand interfaces, the Garson’s Algorithm was adopted to quantitatively assess the relative significance for the input parameters on the long-term creep shear mechanical properties of the interfaces. The formula for Garson’s Algorithm [59,60] is presented in Equation (6), and the calculated relative significance for the input parameters is depicted in Figure 9.

$$R_{ik} = \frac{\sum_{j=1}^L (|W_{ij}W_{jk}| / \sum_{r=1}^N |W_{rj}|)}{\sum_{i=1}^N \sum_{j=1}^L (|W_{ij}W_{jk}| / \sum_{r=1}^N |W_{rj}|)} \quad (6)$$

where R_{ik} indicates the parameter relative importance; W_{ij}, W_{jk} indicates the connection weight between the input and hidden layers as well as the hidden and output layers; N indicates the input parameter number; and M indicates the output parameter number.

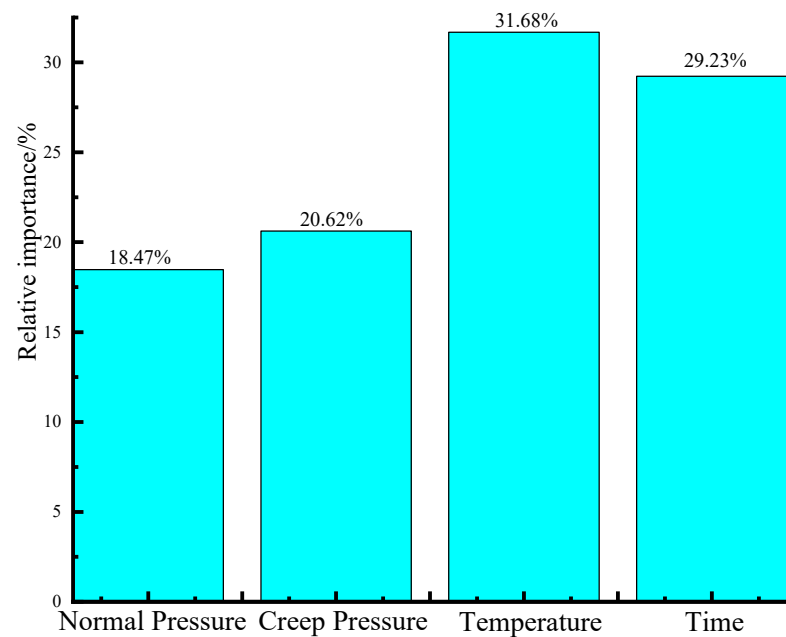


Figure 9. The sensitivity analysis results.

According to Figure 9, temperature has the highest influence on the long-term creep shear mechanical properties of textured geomembrane–sand interfaces, with the relative significance of 31.68%. It is followed by time, with the percentage of 29.23%. In comparison, normal pressure and creep shear pressure have a relatively small impact on the creep shear mechanical response of the interfaces, with the proportions of 18.47% and 20.62%, respectively.

6. Case Study

To verify the reliability of the established machine learning models, a case study is carried out to assess the creep shear displacement of a textured geomembrane–silica sand interface in specific normal pressure, creep shear pressure, temperature, and time by adopting the developed BPANN model. The predicting results were compared with the creep shear displacement measured in the laboratory tests to verify the precision of this model. The specific test conditions and the corresponding input parameters for the BPANN model are listed in Table 4. The predicted creep shear displacement of the interface by using the BPANN model and the measured value in the physical test is presented in Figure 10.

Table 4. The test conditions and the corresponding input values.

Test Condition	Value	Input Value
Temperature	50 °C, 90 °C	50, 90
Time	2000 min, 4000 min	2000, 4000
Normal stress	60 kPa, 100 kPa	60, 100
Creep shear pressure	70% of the peak shear strength	70

According to Figure 10, the assessed creep shear displacements of the textured geomembrane–silica sand interface in the specific normal pressure, creep shear pressure, temperature, and time obtained from the BPANN model are similar to the measured creep shear displacements in the physical test. It indicates the developed machine learning model can estimate the temperature-dependent long-term creep shear mechanical response of the textured geomembrane–silica sand interfaces precisely.

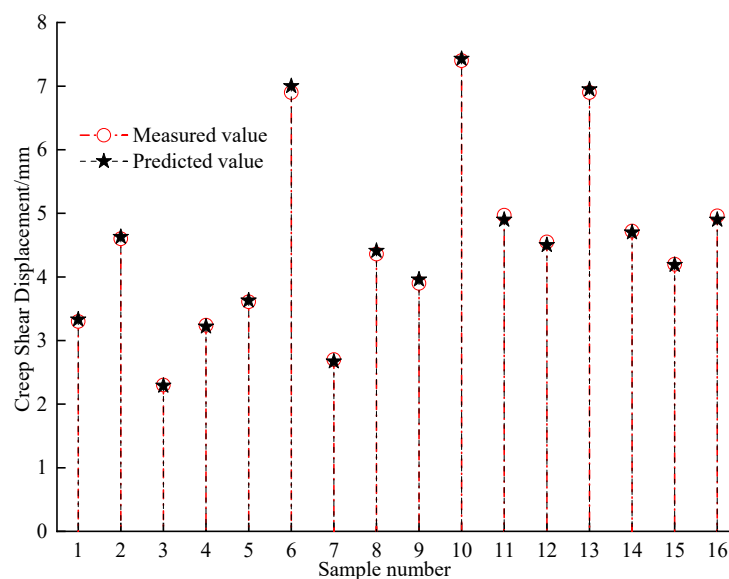


Figure 10. The measured and predicted creep shear displacement.

7. Limitation

Despite the research presenting precious findings, there are limitations for this research. (1) The adopted database for establishing the machine learning models consists of 27,000 datasets, which is not less. However, it still has the room to further enlarge, and the forecasting performance for the machine learning models can be continually enhanced if the bigger database is available; and (2) the influence factors on the creep shear mechanical properties of textured geomembrane–silica sand interfaces are many. Except for the selected input parameters in this research, the properties of textured geomembrane and sand also have impacts on the mechanical response. It should be considered in the future investigation.

8. Conclusions

In this paper, by adopting the self-developed large temperature-controlled interface shear apparatus, a series of long-term creep shear tests on textured geomembrane–silica sand interfaces in different temperatures, normal pressure, and creep shear pressure were conducted. Based on the physical test results, the machine learning models for assessing the temperature-dependent long-term creep shear mechanical response of textured geomembrane–silica sand interfaces were established by using three different machine learning algorithms of BPANN, SVM, and ELM. Then, the forecasting outcomes of the different machine learning models were compared and analyzed. After that, by using the optimal machine learning model combined with Garson’s Algorithm, the sensitivity analysis was carried out to determine the relative significance of the input parameters on influencing the creep shear mechanical properties of the interfaces. In the end, the case study was conducted to verify the reliability for the results forecasted from the constructed machine learning model by comparing with the measured mechanical response of the interfaces in the physical tests.

The main research outcomes are as follows: The hidden layer joint number has a considerable impact on the assessing precision of the BPANN and ELM models. Compared to SVM and ELM model, the BPANN model has a superior performance in forecasting the temperature-dependent long-term creep shear mechanical response of textured geomembrane–silica sand interfaces based on the assessment indexes of RMSE, R, WI, and MAPE. The sensitivity analysis indicates the influence of temperature on the creep shear mechanical properties of textured geomembrane–silica sand interfaces is the largest, followed by time, and creep shear pressure and normal pressure have relative low influence.

For future research directions, it is advisable to consider the incorporation of additional factors into the modeling process, such as wet–dry cycling and the characterization of geomembranes (whether they are smooth or textured). Furthermore, the application of 3D printing technology can be explored to fabricate geomembranes with varying protrusion heights. Subsequent experiments can be conducted to gather extensive data, thus facilitating the expansion of the machine learning model’s database. These steps are essential in the development of a machine learning model with improved accuracy and enhanced generalization capabilities for the prediction of long-term creep mechanical properties at geomembrane–soil interfaces.

Author Contributions: Conceptualization, Z.C.; Investigation, H.W. and H.H.; Resources, Z.C.; Data curation, H.H. and Y.Z.; Writing—original draft, Z.C.; Writing—review & editing, Z.C., H.W. and Y.Z.; Visualization, H.W., T.D. and Y.Z.; Supervision, T.D.; Funding acquisition, Z.C. All authors have read and agreed to the published version of the manuscript.

Funding: This research was funded by the consistent support of the National Natural Science Foundation of China (No. 52301327). The paper is also sponsored by the 2022 Open Project of Failure Mechanics and Engineering Disaster Prevention, Key Lab of Sichuan Province (No. FMEDP202209); the Shanghai Sailing Program (No. 22YF1415800, No. 23YF1416100); Finally, this project is also funded by the Shanghai Natural Science Foundation (No. 23ZR1426200), the China Postdoctoral Science Foundation (No. 2023M730929), The Shanghai Soft Science Key Project (No. 23692119700), the Key Laboratory of Ministry of Education for Coastal Disaster and Protection, Hohai University (No. 202302), and the Key Laboratory of Estuarine & Coastal Engineering, Ministry of Transport (No. KLECE202302).

Institutional Review Board Statement: Not applicable.

Informed Consent Statement: Not applicable.

Data Availability Statement: In this paper, all the data, models, and code used during the study appear in the submitted article.

Conflicts of Interest: The authors declare no conflict of interest.

References

1. Araújo, G.L.S.; Sánchez, N.P.; Palmeira, E.M.; Almeida, M.D.G.G.D. Influence of micro and macroroughness of geomembrane surfaces on soil-geomembrane and geotextile-geomembrane interface strength. *Geotext. Geomembr.* **2022**, *50*, 751–763. [[CrossRef](#)]
2. Abdelaal, F.; Solanki, R. Effect of geotextile ageing and geomembrane surface roughness on the geomembrane-geotextile interfaces for heap leaching applications. *Geotext. Geomembr.* **2022**, *50*, 55–68. [[CrossRef](#)]
3. Zainab, B.; Wireko, C.; Li, D.; Tian, K.; Abichou, T. Hydraulic conductivity of bentonite-polymer geosynthetic clay liners to coal combustion product leachates. *Geotext. Geomembr.* **2022**, *49*, 1129–1138. [[CrossRef](#)]
4. Zainab, B.; Tian, K. Effect of effective stress on hydraulic conductivity of bentonite–polymer geosynthetic clay liners to coal combustion product leachates. *Environ. Geotech.* **2021**, *40*, 1–12. [[CrossRef](#)]
5. Li, D.; Tian, K. Effects of prehydration on hydraulic conductivity of bentonite-polymer geosynthetic clay liner to coal combustion product leachate. *Geo-Congress* **2022**, *2022*, 568–577.
6. Rowe, R.K.; Fan, J. Effect of geomembrane hole geometry on leakage overlain by saturated tailings. *Geotext. Geomembr.* **2021**, *49*, 1506–1518. [[CrossRef](#)]
7. Rowe, R.K.; Jabin, F. Effect of prehydration, permeant, and desiccation on GCL/Geomembrane interface transmissivity. *Geotext. Geomembr.* **2021**, *49*, 1451–1469. [[CrossRef](#)]
8. Chao, Z.; Shi, D.; Fowmes, G. Mechanical behaviour of soil under drying–wetting cycles and vertical confining pressures. *Environ. Geotech.* **2023**, *1–9*. [[CrossRef](#)]
9. Cui, C.-Y.; Zhang, S.-P.; Yang, G.; Li, X.-F. Vertical vibration of a floating pile in a saturated viscoelastic soil layer overlaying bedrock. *J. Central S. Univ.* **2016**, *23*, 220–232. [[CrossRef](#)]
10. Shu, Z.; Ning, B.; Chen, J.; Li, Z.; He, M.; Luo, J.; Dong, H. Reinforced moment-resisting glulam bolted connection with coupled long steel rod with screwheads for modern timber frame structures. *Earthq. Eng. Struct. Dyn.* **2023**, *52*, 845–864. [[CrossRef](#)]
11. Meng, K.; Cui, C.; Liang, Z.; Li, H.; Pei, H. A new approach for longitudinal vibration of a large-diameter floating pipe pile in visco-elastic soil considering the three-dimensional wave effects. *Comput. Geotech.* **2020**, *128*, 103840. [[CrossRef](#)]
12. Cui, C.; Xu, M.; Xu, C.; Zhang, P.; Zhao, J. An ontology-based probabilistic framework for comprehensive seismic risk evaluation of subway stations by combining Monte Carlo simulation. *Tunn. Undergr. Space Technol.* **2023**, *135*, 105055. [[CrossRef](#)]

13. Cui, C.; Meng, K.; Xu, C.; Liang, Z.; Li, H.; Pei, H. Analytical solution for longitudinal vibration of a floating pile in saturated porous media based on a fictitious saturated soil pile mode. *Comput. Geotech.* **2021**, *131*, 103942. [[CrossRef](#)]
14. Eldesouky, H.; Brachman, R. Calculating local geomembrane strains from gravel particle indentations with thin plate theory. *Geotext. Geomembr.* **2023**, *51*, 56–72. [[CrossRef](#)]
15. Francey, W.; Rowe, R.K. Importance of thickness reduction and squeeze-out Std-OIT loss for HDPE geomembrane fusion seams. *Geotext. Geomembr.* **2023**, *51*, 30–42. [[CrossRef](#)]
16. Abdelaal, F.B.; Rowe, R.K. Physical and mechanical performance of an HDPE geomembrane in 10 mining solutions with different pHs. *Can. Geotech. J.* **2023**, *60*, 978–993. [[CrossRef](#)]
17. Zhang, W.; Shi, D.; Shen, Z.; Wang, X.; Gan, L.; Shao, W.; Tang, P.; Zhang, H.; Yu, S. Effect of calcium leaching on the fracture properties of concrete. *Constr. Build. Mater.* **2023**, *365*, 130018. [[CrossRef](#)]
18. Ng, C.W.; Chen, R.; Coo, J.; Liu, J.; Ni, J.; Chen, Y.; Zhan, L.-T.; Guo, H.; Lu, B. A novel vegetated three-layer landfill cover system using recycled construction wastes without geomembrane. *Can. Geotech. J.* **2019**, *56*, 1863–1875. [[CrossRef](#)]
19. Cai, X.; Yuan, J.; Zhou, Z.; Pi, Z.; Tan, L.; Wang, P.; Wang, S.; Wang, S. Effects of hole shape on mechanical behavior and fracturing mechanism of rock: Implications for instability of underground openings. *Tunn. Undergr. Space Technol.* **2023**, *141*, 105361. [[CrossRef](#)]
20. Zhang, X.; Ma, Z.; Wu, Y.; Liu, J. Response of Mechanical Properties of Polyvinyl Chloride Geomembrane to Ambient Temperature in Axial Tension. *Appl. Sci.* **2021**, *11*, 10864. [[CrossRef](#)]
21. Zhou, Z.; Wang, P.; Cai, X.; Cao, W. Influence of Water Content on Energy Partition and Release in Rock Failure: Implications for Water-Weakening on Rock-burst Proneness. *Rock Mech. Rock Eng.* **2023**, *56*, 6189–6205. [[CrossRef](#)]
22. Zhou, Z.; Cai, X.; Li, X.; Cao, W.; Du, X. Dynamic Response and Energy Evolution of Sandstone Under Coupled Static–Dynamic Compression: Insights from Experimental Study into Deep Rock Engineering Applications. *Rock Mech. Rock Eng.* **2020**, *53*, 1305–1331. [[CrossRef](#)]
23. Cui, C.Y.; Meng, K.; Wu, Y.J.; Chapman, D.; Liang, Z. Dynamic response of pipe pile embedded in layered visco-elastic media with radial inhomogeneity under vertical excitation. *Geomech. Eng.* **2018**, *16*, 609–618.
24. Cui, C.; Liang, Z.; Xu, C.; Xin, Y.; Wang, B. Analytical solution for horizontal vibration of end-bearing single pile in radially heterogeneous saturated soil. *Appl. Math. Model.* **2023**, *116*, 65–83. [[CrossRef](#)]
25. Cui, C.; Meng, K.; Xu, C.; Wang, B.; Xin, Y. Vertical vibration of a floating pile considering the incomplete bonding effect of the pile-soil interface. *Comput. Geotech.* **2022**, *150*, 104894. [[CrossRef](#)]
26. Samea, A.; Abdelaal, F.B. Effect of elevated temperatures on the degradation behaviour of elastomeric bituminous geomembranes. *Geotext. Geomembr.* **2023**, *51*, 219–232. [[CrossRef](#)]
27. Cui, C.; Zhang, S.; Chapman, D.; Meng, K. Dynamic impedance of a floating pile embedded in poro-visco-elastic soils subjected to vertical harmonic loads. *Geomech. Eng.* **2018**, *15*, 793–803.
28. Abdelaal, F.; Morsy, M.; Rowe, R.K. Long-term performance of a HDPE geomembrane stabilized with HALS in chlorinated water. *Geotext. Geomembr.* **2019**, *47*, 815–830. [[CrossRef](#)]
29. Mhamed, M.; Sutcliffe, R.; Sun, X.; Feng, J.; Retta, E.A. Arabic sentiment analysis using GCL-based architectures and a customized regularization function. *Eng. Sci. Technol. Int. J.* **2023**, *43*, 101433.
30. Janiesch, C.; Zschech, P.; Heinrich, K. Machine learning and deep learning. *Electron. Mark.* **2021**, *31*, 685–695. [[CrossRef](#)]
31. Cazzuffi, D.; Giofrè, D. Lifetime assessment of exposed PVC-P geomembranes installed on Italian dams. *Geotext. Geomembr.* **2020**, *48*, 130–136. [[CrossRef](#)]
32. Dong, Y.; Cui, L.; Zhang, X. Multiple-GPU parallelization of three-dimensional material point method based on single-root complex. *Int. J. Numer. Meth. Eng.* **2022**, *123*, 1481–1504. [[CrossRef](#)]
33. Zhao, G.; Wu, T.; Ren, G.; Zhu, Z.; Gao, Y.; Shi, M.; Ding, S.; Fan, H. Reusing waste coal gangue to improve the dispersivity and mechanical properties of dispersive soil. *J. Clean. Prod.* **2023**, *404*, 136993. [[CrossRef](#)]
34. Anjana, R.; Keerthana, S.; Arnepalli, D.N. Coupled effect of UV ageing and temperature on the diffusive transport of aqueous, vapour and gaseous phase organic contaminants through HDPE geomembrane. *Geotext. Geomembr.* **2023**, *51*, 316–329. [[CrossRef](#)]
35. Wang, F.; Zhang, D.; Huang, H.; Huang, Q. A phase-field-based multi-physics coupling numerical method and its application in soil–water inrush accident of shield tunnel. *Tunn. Undergr. Space Technol.* **2023**, *140*, 105233. [[CrossRef](#)]
36. Wang, F.; Huang, H.; Zhang, D.; Zhou, M. Cracking feature and mechanical behavior of shield tunnel lining simulated by a phase-field modeling method based on the spectral decomposition. *Tunn. Undergr. Space Technol.* **2021**, *119*, 104246. [[CrossRef](#)]
37. Wang, F.; Zhou, M.; Shen, W.; Huang, H.; He, J. Fluid-solid-phase multi-field coupling modeling method for hydraulic fracture of saturated brittle porous materials. *Eng. Fract. Mech.* **2023**, *286*, 109231. [[CrossRef](#)]
38. Zargar, O.; Pharr, M.; Muliana, A. Modeling and simulation of creep response of sorghum stems: Towards an understanding of stem geometrical and material variations. *Biosyst. Eng.* **2022**, *217*, 1–17. [[CrossRef](#)]
39. Li, D.; Jiang, Z.; Tian, K.; Ji, R. Prediction of hydraulic conductivity of sodium bentonite GCLs by machine learning approaches. *Environ. Geotech.* **2023**, 1–17. [[CrossRef](#)]
40. Zhang, W.; Shi, D.; Shen, Z.; Zhang, J.; Zhao, S.; Gan, L.; Li, Q.; Chen, Y.; Tang, P. Influence of chopped basalt fibers on the fracture performance of concrete subjected to calcium leaching. *Theor. Appl. Fract. Mech.* **2023**, *125*, 103934. [[CrossRef](#)]
41. Hart, G.L.W.; Mueller, T.; Toher, C.; Curtarolo, S. Machine learning for alloys. *Nat. Rev. Mater.* **2021**, *6*, 730–755. [[CrossRef](#)]

42. Chao, Z.; Dang, Y.; Pan, Y.; Wang, F.; Wang, M.; Zhang, J.; Yang, C. Prediction of the shale gas permeability: A data mining approach. *Geomech. Energy Environ.* **2023**, *33*, 100435. [[CrossRef](#)]
43. Zhang, W.; Shi, D.; Shen, Z.; Shao, W.; Gan, L.; Yuan, Y.; Tang, P.; Zhao, S.; Chen, Y. Reduction of the calcium leaching effect on the physical and mechanical properties of concrete by adding chopped basalt fibers. *Constr. Build. Mater.* **2023**, *365*, 130080. [[CrossRef](#)]
44. Chao, Z.; Shi, D.; Fowmes, G.; Xu, X.; Yue, W.; Cui, P.; Hu, T.; Yang, C. Artificial intelligence algorithms for predicting peak shear strength of clayey soil-geomembrane interfaces and experimental validation. *Geotext. Geomembr.* **2023**, *51*, 179–198. [[CrossRef](#)]
45. Dong, Y.; Wang, D.; Randolph, M.F. Investigation of impact forces on pipeline by submarine landslide using material point method. *Ocean Eng.* **2017**, *146*, 21–28. [[CrossRef](#)]
46. Sabitova, A.; Yarushina, V.M.; Stanchits, S.; Stukachev, V.; Khakimova, L.; Myasnikov, A. Experimental compaction and dilation of porous rocks during triaxial creep and stress relaxation. *Rock Mech. Rock Eng.* **2021**, *54*, 5781–5805. [[CrossRef](#)]
47. Pillai, A.G.; Gali, M.L. Digital image-based performance evaluation of GCL-sand interfaces under repeated shearing. *Geosynth. Int.* **2022**, 1–21. [[CrossRef](#)]
48. Fan, N.; Jiang, J.; Nian, T.; Dong, Y.; Guo, L.; Fu, C.; Tian, Z.; Guo, X. Impact action of submarine slides on pipelines: A review of the state-of-the-art since 2008. *Ocean Eng.* **2023**, *286*, 115532. [[CrossRef](#)]
49. Piegari, E.; De Donno, G.; Melegari, D.; Paoletti, V. A machine learning-based approach for mapping leachate contamination using geoelectrical methods. *Waste Manag.* **2023**, *157*, 121–129. [[CrossRef](#)]
50. Shao, W.; Xiong, Y.; Shi, D.; Xu, X.; Yue, W.; Soomro, M.A. Time dependent analysis of lateral bearing capacity of reinforced concrete piles combined with corrosion and scour. *Ocean Eng.* **2023**, *282*, 115065. [[CrossRef](#)]
51. Sanchez, D.; Gilchrist, D.; Yang, S.; Bandara, K.M.A.S.; Gamage, R.P.; Zheng, W. Experimental characterization of time-dependent mechanical behaviours of frac sand at high compressive stresses and implication on long-term proppant conductivity. *Geomech. Geophys. Geo-Energy Geo-Resour.* **2022**, *8*, 1–18. [[CrossRef](#)]
52. Camarena-Martinez, R.; Lizarraga-Morales, R.A.; Baeza-Serrato, R. Classification of Geomembranes as Raw Material for Defects Reduction in the Manufacture of Biodigesters Using an Artificial Neuronal Network. *Energies* **2021**, *14*, 7345. [[CrossRef](#)]
53. Fleury, M.P.; Kamakura, G.K.; Pitombo, C.S.; Cunha, A.L.B.; da Silva, J.L. Prediction of non-woven geotextiles' reduction factors for damage caused by the drop of backfill materials. *Geotext. Geomembr.* **2023**, *51*, 120–130. [[CrossRef](#)]
54. Wang, H.; Li, L.; Li, J.; Sun, D. Drained expansion responses of a cylindrical cavity under biaxial in situ stresses: Numerical investigation with implementation of anisotropic S-CLAY1 model. *Can. Geotech. J.* **2023**, *60*, 198–212. [[CrossRef](#)]
55. Scholkopf, B.; Smola, A.J. *Learning with Kernels: Support Vector Machines, Regularization, Optimization, and Beyond*; MIT Press: Cambridge, MA, USA, 2001.
56. Zang, W.; Zheng, Y.; Zhang, Y.; Lin, X.; Li, Y.; Fernandez-Rodriguez, E. Numerical Investigation on a Diffuser-Augmented Horizontal Axis Tidal Stream Turbine with the Entropy Production Theory. *Mathematics* **2022**, *11*, 116. [[CrossRef](#)]
57. Witten, I.H.; Frank, E.; Hall, M.A. *Data Mining Fourth Edition: Practical Machine Learning Tools and Techniques*; Morgan Kaufmann Publishers Inc.: San Francisco, CA, USA, 2016.
58. Otchere, D.A.; Ganat, T.O.A.; Gholami, R.; Ridha, S. Application of supervised machine learning paradigms in the prediction of petroleum reservoir properties: Comparative analysis of ANN and SVM models. *J. Pet. Sci. Eng.* **2020**, *200*, 108182. [[CrossRef](#)]
59. Das, S.K.; Basudhar, P.K. Undrained lateral load capacity of piles in clay using artificial neural network. *Comput. Geotech.* **2006**, *33*, 454–459. [[CrossRef](#)]
60. Kanungo, D.P.; Sharma, S.; Pain, A. Artificial Neural Network (ANN) and Regression Tree (CART) applications for the indirect estimation of unsaturated soil shear strength parameters. *Front. Earth Sci.* **2014**, *8*, 439–456. [[CrossRef](#)]

Disclaimer/Publisher's Note: The statements, opinions and data contained in all publications are solely those of the individual author(s) and contributor(s) and not of MDPI and/or the editor(s). MDPI and/or the editor(s) disclaim responsibility for any injury to people or property resulting from any ideas, methods, instructions or products referred to in the content.